

Article www.acsaem.org

# Controlling the Relative Fluxes of Protons and Oxygen to Electrocatalytic Buried Interfaces with Tunable Silicon Oxide **Overlayers**

Marissa E. S. Beatty, Eleanor I. Gillette, Alexis T. Haley, and Daniel V. Esposito\*



Cite This: ACS Appl. Energy Mater. 2020, 3, 12338-12350



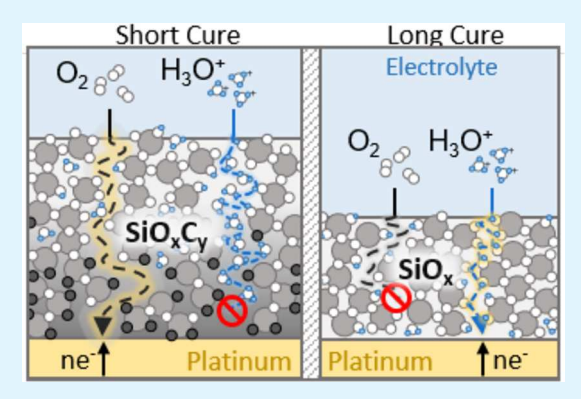
**ACCESS** 

III Metrics & More



Supporting Information

**ABSTRACT:** Modifying an electrocatalyst surface by encapsulating it with a nanoscale oxide membrane is an attractive approach for improving its activity, stability, and selectivity. However, little is known about how the composition and structure of such overlayers impact the properties and performance of the underlying electrocatalyst. The results presented herein demonstrate that the density and carbon content of carbon-modified silicon oxide  $(SiO_xC_y)$  overlayers can be systematically varied using a roomtemperature photochemical conversion process to precisely control the flux of protons and molecular oxygen (O2) to the buried interface of an encapsulated platinum electrode. Correlations between species permeabilities, overlayer composition, and overlayer structure show that proton transport is greatly enhanced as the carbon content decreases and overlayer density increases, while the inverse trend is observed for O2. These



observations are found to be consistent with O<sub>2</sub> diffusing through the free volume in the SiO<sub>x</sub>C<sub>y</sub> matrix, while proton diffusion proceeds through a facilitated transport mechanism associated with the hydrogen bond network of silicon oxide moieties. Importantly, this study indicates that overlayer composition can be a potentially powerful control knob for tuning the fluxes of redox species to active sites as well as modifying local properties at electrocatalytic buried interfaces.

KEYWORDS: electrocatalysis, buried interface, silicon oxide, overlayer, hydrogen evolution reaction, oxygen reduction reaction

# 1. INTRODUCTION

Electrocatalytic technologies like electrolyzers and fuel cells are expected to play key roles in a sustainable energy future based on their ability to convert renewable electricity into storable chemicals and fuels. However, several challenges still remain in the development of highly active, selective, and stable electrocatalytic materials required for improving the performance of these technologies. 1,2 Traditionally, approaches for improving electrocatalyst performance have included controlling electrocatalyst composition, 3-5 nanostructure, 6-8 and support effects. Great strides have been made to improve electrocatalyst performance and decrease the loading of platinum group metals, but many of the aforementioned approaches often encounter upper performance limits due to scaling relations associated with species binding energies at conventional electrocatalyst/electrolyte interfaces based on a single electrocatalyst material. 10,11

Another proposed solution toward improving electrocatalytic activity and stability is to encapsulate the active catalysts within an ultrathin, semipermeable oxide overlayer, creating an architecture known as a membrane-coated electrocatalyst (MCEC).<sup>12</sup> In these electrocatalysts, reactant species diffuse through the overlayer to react at the buried catalytic interface. Previous work with Pt-based MCECs has

shown that encapsulation by oxide overlayers can improve nanoparticle stability, 13,14 impart poisoning resistance, 15 increase catalytic activity, 16,17 and increase selectivity by blocking undesirable side reactions. 18,19 The degree to which these overlayers affect electrocatalyst performance is influenced by both the oxide membrane and catalyst materials, with selective species transport, 15,20 intermediate removal, 17 and catalyst stabilization<sup>21</sup> being proposed as possible explanations for the improvements seen in activity and stability. In all cases, overlayer thickness is of critical importance in determining MCEC performance; the overlayer should be thick enough to impart the desirable selective transport properties but cannot be so thick such that it creates large concentration overpotential losses. 12,15

While numerous studies have explored the effects of active catalyst composition<sup>22</sup> and overlayer thickness<sup>15,17</sup> on MCEC

Received: September 24, 2020 Accepted: November 25, 2020 Published: December 9, 2020





performance, very few studies have identified clear relationships between the composition and transport properties of the nanoscale overlayers. Previous studies have demonstrated that changing the siloxane precursor composition  $^{13,23}$  or composite structure  $^{24}$  of silicon oxide  $(\mathrm{SiO}_x)$  overlayers greatly alters their physical and chemical properties, which subsequently influenced the performance of  $\mathrm{SiO}_x$ -encapsulated Pt electrodes for the alcohol oxidation  $^{13}$  and oxygen reduction reactions (ORRs).  $^{23,24}$  From these observations, an opportunity exists to more precisely control MCEC selectivity for different redox species. Rather than increasing the thickness of an overlayer, which decreases the flux of both the desired and undesired species, altering the overlayer composition could serve a straightforward way to control the transport selectivity toward a desired species without decreasing its flux.

In the current study, we employ well-defined carbonmodified, SiO<sub>x</sub>-encapsulated Pt thin film electrodes (SiO<sub>x</sub>C<sub>y</sub>I Pt) as a platform for systematically exploring the influence of overlayer composition on the transport and electrochemical properties of Pt-based MCEC architectures. SiO<sub>x</sub> was selected as the overlayer material for this study based on its chemical stability under acidic and pH-neutral conditions, 25 permeability to many species relevant to electrochemical energy applications, 3,15,17 and inactivity as an electrocatalyst by itself given that pure SiO<sub>2</sub> is electronically insulating. This latter characteristic can be beneficial for suppressing electrochemical reactions from occurring on the outer surface of the oxide, thereby promoting electrochemical reactions at the buried interface. Building off of our prior work with SiO<sub>x</sub>|Pt MCECs,  $^{15,17,22}$  amorphous SiO<sub>x</sub>C<sub>y</sub> overlayers were deposited onto planar, polycrystalline Pt electrodes using a roomtemperature ultraviolet-ozone (UV-ozone) wet chemical method that has been previously described.<sup>26</sup> Briefly, poly-(dimethylsiloxane) (PDMS) was deposited onto the Pt electrode and exposed to ultraviolet light, which triggers photochemical decomposition of O2 in air to form ozone and oxygen radicals. These species then permeate into the overlayer and convert the methyl groups in the PDMS into gaseous CO2 and H2O byproducts, which then diffuse out of the overlayer, gradually converting the layer's composition and structure from that of PDMS to a fully cured state after 2 h with composition similar to SiO<sub>2</sub>. <sup>26,27</sup> As illustrated in Figure 1, limiting the duration of the UV-ozone curing process allows for the synthesis of partially converted  $SiO_xC_y$  overlayers



**Figure 1.** Key steps in the photochemical deposition process for fabricating  $SiO_xC_y$ -encapsulated Pt thin films. In step 3, the length of the UV-ozone treatment is shown to impact the density, thickness, and composition of the  $SiO_xC_y$  overlayers.

characterized by compositions, densities, and thicknesses that fall in between those of PDMS and fully cured SiO<sub>x</sub>.

Variations in the composition and structure of an MCEC overlayer are expected to have significant effects on its transport properties, as evidenced by previous studies that show how O<sub>2</sub> selectivity and permeability are highly sensitive to the length of exposure to either plasma or ozone in PDMSderived SiO<sub>x</sub> gas diffusion membranes. 28-31 Similarly, researchers have reported large differences in proton permeabilities through siloxane polymers and SiO<sub>2</sub>, <sup>32-3</sup>432-34 suggesting that proton transport may also be manipulated by gradually varying the composition of a membrane between SiO<sub>2</sub> and its siloxane precursor. Given that protons and oxygen are commonly encountered redox species that are relevant to a large number of industrially important electrochemical reactions, selectively controlling the relative fluxes of these reactants presents an enticing opportunity to modulate the rates of electrochemical reactions involving these species relative to competing reactions.

This study focuses on altering  $SiO_xC_y$  overlayer composition by varying the duration of the UV-ozone conversion process and quantifying the resultant effects on species transport through the overlayer, as well as the electrochemical characteristics of the buried interface. In the first part of this study, a variety of characterization methods are used to investigate how different physical and chemical properties of the overlayer are altered as a function of the UV-ozone cure time. These properties are then related to electrochemical performance toward the hydrogen evolution reaction (HER) and the oxygen reduction reaction (ORR) under mass transport limiting conditions. HER and ORR limiting current densities are used as inputs to steady-state diffusion models to estimate species permeabilities within the  $SiO_xC_y$  overlayers as a function of cure time. From these results, relationships between overlayer characteristics and species permeabilities are identified and can be used to guide the design of MCECs with optimized fluxes of protons and/or O<sub>2</sub>.

# 2. EXPERIMENTAL SECTION

2.1. Electrode Fabrication. Monocrystalline degenerately doped p<sup>+</sup>Si(100) wafers (Prime-grade p<sup>+</sup>Si, resistivity <0.005 Ω cm, 500– 550  $\mu$ m thick, WRS materials) were used as conductive substrates. Two nanometers of titanium and 50 nm of platinum at 99.9% purity were sequentially deposited by electron-beam deposition under high vacuum ( $<5 \times 10^{-8}$  Torr) at a rate of 0.5 and 1 Å s<sup>-1</sup>, respectively. The deposited wafers were then washed and sonicated for 5 min sequentially in acetone, methanol, isopropanol, and deionized water. A solution of high-molecular-weight trimethyl siloxy-terminated poly(dimethylsiloxane) (PDMS) in toluene (3.0 mg mL<sup>-1</sup>) was spin-coated onto the PtlTilp+Si substrates for 2.5 min at 4000 rpm. The PDMS-coated electrodes were then dried under vacuum (25 in Hg) at 90  $^{\circ}\text{C}$  for 1 h before undergoing treatment in a UV-ozone chamber (UVOCS, T10X10/OES) to convert the PDMS to SiO<sub>x</sub>C<sub>y</sub>. Replicate samples were fabricated in all cases to ensure reproducibility. Electrical contacts were attached by soldering a copper wire onto the back of the silicon substrate with indium solder, using a soldering iron temperature of 218 °C. The geometric area of the electrode was defined using 3 M electroplater's tape, resulting in a circular 0.246 cm<sup>2</sup> opening through which the electrocatalytic surface was exposed to the electrolyte.

**2.2. Material Characterization.**  $SiO_xC_y$  overlayer thicknesses were measured using a J.A. Woollam  $\alpha$ -SE ellipsometer. The thicknesses of  $SiO_xC_y$  overlayers in the  $SiO_x|Pt|Ti|p^+Si$  samples were determined by sequentially fitting the raw data using a Cauchy model with optical constants derived for  $SiO_2$  (n=1.44),  $^{35}$  and substrate

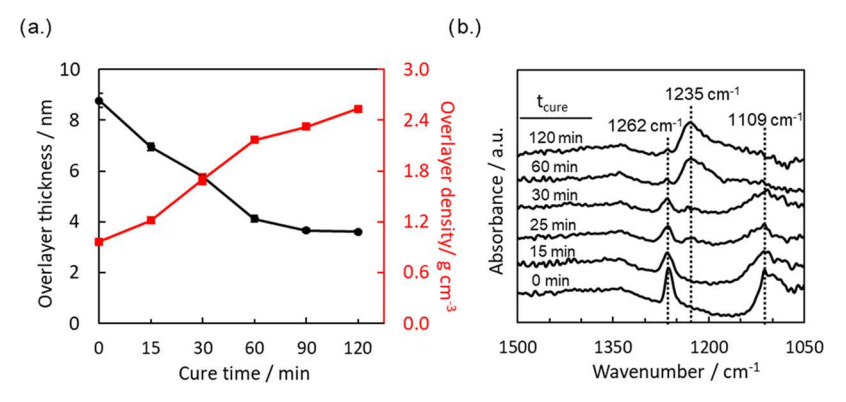


Figure 2. (a) Thicknesses (black curve) and density (red curve) of  $SiO_xC_y$  overlayers deposited on Pt thin films as a function of the total UV–ozone cure time. Overlayer thicknesses were measured by ellipsometry and used as inputs to calculate the overlayer density as described in the Supporting Information. Error bars represent 95% confidence intervals. (b) ATR-FTIR of  $Si-Pt-SiO_xC_y$  samples treated for varying cure times.

thicknesses determined from fitting bare control samples lacking  $\mathrm{SiO}_x C_y$  overlayers. A separate Cauchy model using optical constants for pure PDMS  $(n=1.39)^{36}$  was also used to determine the  $\mathrm{SiO}_x C_y$  thickness for all samples, which reported deviations of up to  $\approx 5\%$  from the values determined using the pure  $\mathrm{SiO}_2$  model, as shown in Figure S4.

X-ray photoelectron spectroscopy (XPS) measurements were made with a PHI XPS system at pressures  $<2\times10^{-10}$  Torr using a monochromatic Al K $\alpha$  source (15 kV, 20 mA) and a charge neutralizer, tilted to  $54.7^{\circ}$  relative to the detector. Multiplex spectra are shown as averages of three measurements and were fit using XPSPEAK software applying Shirley's algorithm for background subtraction. All peaks were calibrated such that the Pt  $4f_{7/2}$  peaks were centered on 71.2 eV.<sup>37</sup> Atomic ratios were calculated by normalizing intensity by each element's atomic sensitivity factor (ASF).<sup>38</sup> Contact angles were measured on a standard goniometer (ramé-hart instrument co.) using  $10~\mu$ L of deionized water at standard lab conditions. All droplet images were fit with measured angles using DROPimage (v2.8.05) software.

Surface topography and roughness were measured with a Bruker Dimension Icon atomic force microscope (AFM) in air using a ScanAsyst silicon tip on a nitride cantilever with a 2 nm nominal tip radius and a spring force constant of 0.4 N m<sup>-1</sup>. Measurements were performed in peak force nanomechanical mapping mode using a scan rate of 0.977 Hz and a resonant frequency of 70 kHz. Secondary electron (SE) images of the sample surfaces were acquired using a Zeiss Sigma VP Schottky thermal field emission scanning electron microscope (SEM) using a beam voltage of 2.0 kV.

Fourier transform infrared (FTIR) spectra were collected on a Jasco FTIR-6800 spectrometer with a nitrogen-cooled MCT-A detector and a Pike Technologies GladiATR accessory with a germanium attenuated total reflection (ATR) crystal. Spectra were collected from 950 to 4000 cm $^{-1}$  with a resolution of 4 cm $^{-1}$ , and 128 scans were averaged for each sample to improve the signal-to-noise ratios. All data are reported as absorbance ( $A = -\log(I_{\rm sample}/I_{\rm reference}))$ , where reference spectra ( $I_{\rm reference}$ ) are collected from Pt-coated silicon wafers prepared in the same way as the SiO $_{x}$ -coated samples. Baseline and CO $_{2}$  and H $_{2}$ O corrections were performed in Jasco Spectra Analysis, while peak fitting and integration were performed using Gaussian fits in Origin 2017.

2.3. Electrochemical Measurements. Electrolytes for all electrochemical measurements were prepared from concentrated sulfuric acid ( $H_2SO_4$ , Certified ACS plus, Fischer Scientific), sodium sulfate ( $Na_2SO_4$ , ACS grade, Sigma-Aldrich), and 18 M $\Omega$  deionized water (Millipore, Milli-Q Direct 8). Electrolytes with lower concentrations of sulfuric acid were balanced with sodium sulfate such that the total ionic concentration equaled 500 mM to ensure uniform electrolyte conductivity. pH measurements for all electroanalytical experiments were taken with a benchtop pH meter (Fisher Science Education, S90526), using a three-point calibration from 1.69, 4.01, and 7.00 standard buffers (Oaklon). Electrochemical measure-

ments were conducted using either an SP-200 or SP-300 BioLogic potentiostat and carried out in a standard three-neck round-bottom glass cell with a commercial AglAgCl (3 M KCl) reference electrode ( $E^{\circ}$  = 0.21 V vs normal hydrogen electrode (NHE), Hach, E21M002) and a carbon rod (Saturn Industries) counter electrode. All electrolytes were first deaerated by purging with nitrogen gas ( $N_2$ ) for 20 min before experiments. For conditions that required  $N_2$  gas as a reactant species (i.e., ORR), electrolytes were purged with pure  $N_2$  (ultrahigh purity (UHP)) for 20 min prior to measurement to saturate the solution. During measurement,  $N_2$  was bubbled continuously into solution at a 0.5 L min $^{-1}$  flow rate using a sparge to dissipate any large bubbles. All current densities were normalized with respect to the average geometric area of the exposed electrode.

Initial cyclic voltammetries (CVs) were taken in a supporting electrolyte for 10 cycles from 0.05 to 0.8 V vs reversible hydrogen electrode (RHE) at 25 mV s<sup>-1</sup> preceding all electrochemical measurements. Electrochemically active surface area (ECSA) was calculated by integrating the area from 0.05 to 0.4 V vs RHE from CVs in 0.5 M H<sub>2</sub>SO<sub>4</sub>, subtracting out the charge contributed by the electrochemical double layer over the same region. This area was then divided by 210  $\mu$ C cm<sup>-2</sup>, <sup>39</sup> the accepted value of the charge per area of polycrystalline Pt for proton adsorption/desorption, to obtain a final, normalized ECSA for samples of various cure times. Linear sweep voltammetry (LSV) measurements studying the HER were measured at 10 mV  $\rm s^{-1}$  between 0.8 and  $\rm -0.5~V$  vs RHE in 5 mM H<sub>2</sub>SO<sub>4</sub>, balanced with 495 mM sodium sulfate (Na<sub>2</sub>SO<sub>4</sub>, ACS grade, Sigma-Aldrich) to maintain a constant electrolyte conductivity for all measurements. Background LSVs used for proton permeability analysis were taken over the same potential window and scan rate as the experimental HER LSVs in pH 7.0 Na<sub>2</sub>SO<sub>4</sub>. CVs used to analyze steady-state limiting current for the ORR were cycled between 1.2 and -0.02 V vs RHE for five times at 10 mV s<sup>-1</sup>. Measurements were taken on identical samples in the absence of dissolved O2 to compare background signal and show no substantial differences between samples. Following all experiments, samples were lightly rinsed with DI and stored in a desiccated environment prior to postexperimental characterization.

Limiting current densities used for permeability calculations were taken as averages between -0.2 and -0.5 V vs RHE for the HER and 0.5 and 0.2 V vs RHE for the ORR. Error bars for permeability were calculated using two-sided, 95% confidence intervals based on two to three repeat measurements, accounting for error propagated from the uncertainties in ellipsometry determined in overlayer thickness, as well as uncertainties contributed by noise in the limiting current over the aforementioned potential ranges for each respective reaction. Similarly, calculated densities and Si–Si spacing estimates also accounted for error propagated from deviations in the ellipsometry-determined overlayer thickness.

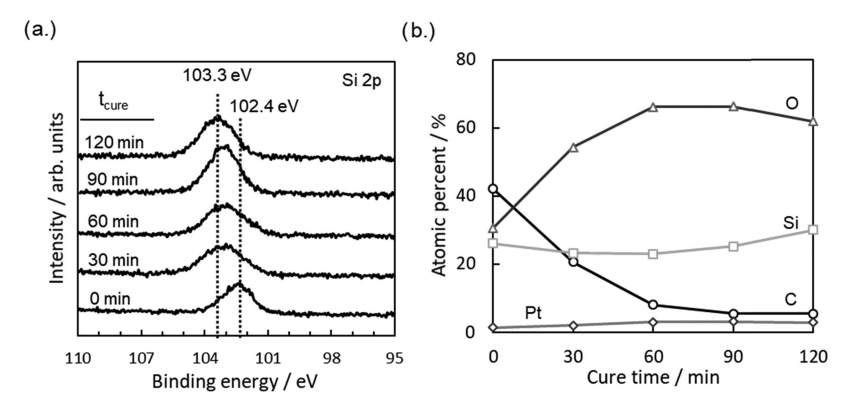


Figure 3. (a) Si 2p spectra and (b) elemental composition obtained from XPS measurements for as-made  $SiO_xC_y|Pt$  samples based on a 5 nm target overlayer thickness that were treated with various UV-ozone cure times ( $t_{cure}$ ). Spectra were obtained using an emission angle of 54.7° relative to the detector.

# 3. RESULTS AND DISCUSSION

3.1. Characterizing the Structure and Composition of  $SiO_xC_v$  Overlayers. To determine how overlayer thickness changes as a function of cure time, a single sample with an initial PDMS layer thickness of 8.8 nm was successively cured in the UV-ozone chamber for 15-30 min increments, using ellipsometry to monitor the thickness in between each curing step. As seen in Figure 2a, the overlayer thickness initially decreased linearly with cure time, shrinking to 47% of the original thickness after the first 60 min, after which the thickness only decreased an additional 12% before reaching a final value of 3.6 nm. This observation indicates that most of the overlayer conversion occurs during the first 60 min, consistent with previous studies of SiO<sub>x</sub>C<sub>y</sub> overlayers deposited on gas diffusion membranes. 26,27 As described in Section SIII, Supporting Information (SI), the density of SiO<sub>x</sub>C<sub>y</sub> overlayers was calculated using the ellipsometry-determined overlayer thicknesses and XPS-determined composition measured at each cure time. Figure 2a shows that overlayers treated for the entire 120 min reach a final density of 2.56 g cm<sup>-3</sup>, which is significantly higher than the density of PDMS (0.965 g cm<sup>-3</sup>)<sup>40</sup> and amorphous type II silica (2.20 g cm<sup>-3</sup>)<sup>41</sup> but less than the density of pure  $\alpha$ -quartz (2.648 g cm<sup>-3</sup>). AFM and SEM measurements of fully cured overlayers ( $t_{\text{cure}} = 120 \text{ min}$ ) further confirm that the SiOx is smooth, continuous, and free of any holes or imperfections, with a surface root-mean-square (RMS) roughness of 0.55  $\pm$  0.17 nm, consistent with previously reported roughness values (Figures S1 and S2).<sup>22</sup>

ATR-FTIR spectra of the  $SiO_xC_y$  overlayers are provided in Figure 2b and reveal that the as-deposited PDMS ( $t_{cure} = 0$ min) closely matches the expected spectra for bulk PDMS, 43 with the peak at ≈1262 cm<sup>-1</sup> being assigned to the methyl stretch and the vibrational modes centered at ≈1072 and 1109 cm<sup>-1</sup> being assigned to the asymmetric and symmetric stretching modes, respectively, of the Si-O-Si backbone in PDMS. These peaks are located at slightly lower wavenumber than bulk PDMS, as is commonly reported for IR characterization of thin PDMS films. 43,44 As treatment time increases, the peaks associated with the methyl stretch decrease in intensity, reflecting the loss of methyl groups in PDMS after exposure to reactive oxygen/ozone species. The lack of other significant carbon peaks suggests that the ozone treatment removes methyl groups without significant production of other partially oxidized carbonyl species, which would absorb strongly in the infrared if present. 45 Concurrently, the position

of the methyl stretch peak shifts toward higher wavenumbers, which has been previously observed in substituted siloxanes when fewer methyl groups are present.<sup>43</sup>

The other major changes observed by FTIR relate to the silicon-oxygen bonding. As the overlayers are further oxidized and carbon is removed, the characteristic PDMS Si-O-Si stretching peaks at 1072 and 1109 cm<sup>-1</sup> decrease in total area and shift to higher wavenumbers, signifying a transition to a more rigid, interlinked structure with more inorganic character. 46 Concurrently, a sharp transition is observed after 30 min of ozone exposure as the Si-O-Si vibration associated with PDMS drops completely below the detection limit and a peak appears at  $\approx 1235$  cm<sup>-1</sup>, which can be assigned to the longitudinal optical (LO) phonon mode of Si-O-Si. This LO phonon has previously been observed for very thin amorphous silicon oxide films<sup>47,48</sup> but is not seen in highly defective silica thin films lacking a continuous network of Si-O bonds.<sup>4</sup> Thus, the growth of the LO phonon peak in Figure 3a for longer cure times indicates that SiO<sub>x</sub>C<sub>y</sub> overlayers only develop a continuous SiO, bonding network capable of long-range coupling between Si-O vibrational modes after 30-60 min of cure time. Concurrently, the SiO<sub>x</sub>C<sub>y</sub> overlayers subjected to longer cure times do not exhibit a peak associated with the transverse optical (TO) phonon mode of Si-O-Si, consistent with previous studies analyzing amorphous silica films with thicknesses less than 10 nm. 47,4

The chemical composition of SiO<sub>x</sub>C<sub>y</sub>|Pt electrodes was further characterized by X-ray photoelectron spectroscopy (XPS). C 1s, O 1s, Si 2p, and Pt 4f spectra were taken for the samples of 0, 30, 60, 90, and 120 min cure times (Figure S5). As seen in Figure 3a, the 0 min sample shows a Si  $2p_{3/2}$  peak centered at 102.4 eV, which closely matches the reported peak location for Si in pure PDMS of 102.6 eV. 49 As cure time increases, the Si 2p peak center shifts to higher binding energy, reaching a value of 103.3 eV for the fully cured sample. This value is slightly lower than that reported in the literature for SiO<sub>2</sub> (103.7 eV),<sup>50</sup> which could be attributed to trace SiO moieties and/or a small amount of residual carbon. Figure 3b shows that the atomic percent of Si within the SiO<sub>x</sub>C<sub>y</sub> layers remains relatively constant with cure time, reflecting that Si atoms are not volatilized during the UV-ozone conversion process. Meanwhile, a slight increase in Pt signal is observed at longer cure times, which can be explained by the decreasing screening of Pt photoelectrons as the  $SiO_xC_y$  overlayer becomes thinner. In contrast to these minimal changes in Pt and Si contribution, the atomic percent of oxygen (O) and

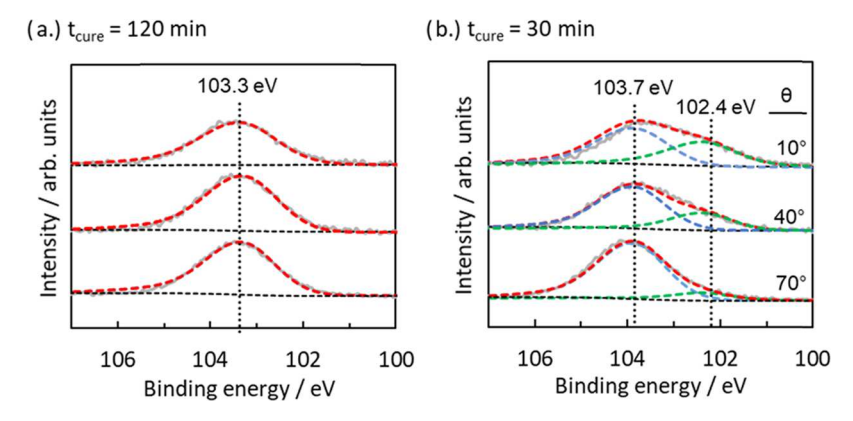


Figure 4. ARXPS measurements for (a) 5.3 nm thick fully cured ( $t_{\text{cure}} = 120 \text{ min}$ ) and (b) 7.6 nm thick partially cured ( $t_{\text{cure}} = 30 \text{ min}$ ) SiO<sub>x</sub>C<sub>y</sub>|Pt samples. Raw Si 2p spectra are shown in gray, along with fitted backgrounds (black dashed curves), individual peak fits (green and blue curves), and curves showing a cumulative fit as a sum of the individual peaks (red curves) at various emission angles ( $\theta$ ), defined as the angle between the detector and surface normal.

carbon (C) significantly increases and decreases, respectively, as methyl groups are converted to CO2 and H2O, and additional oxygen atoms, provided by the reactive oxygen species generated during UV-ozone treatment, are incorporated into the SiO<sub>x</sub> bond network. This is further evidenced by the gradual increase in the O/Si ratio from 1.2 for the initial, uncured PDMS sample to 2.1 for the fully cured sample, with ratios for all other cure times reported in the Supporting Information (Figure S6). Although the final O/Si ratios appear slightly higher than the expected value of 2.0 for SiO<sub>2</sub>, particularly for samples of intermediate cure time, elevated O/ Si ratios are not uncommon for porous, hydrophilic silica xerogels that have been exposed to moisture or CO2 prior to measurement.<sup>51</sup> Thus, the elevated atomic O/Si ratios at intermediate and long cure time samples could be the result of water trapped within the SiO<sub>x</sub>C<sub>y</sub> overlayers that was not completely removed during the UV-ozone conversion process. Similarly, upon completing the full 120 min of curing, only 6.4% residual carbon remains in the overlayer, with some fraction of this likely associated with adventitious carbon adsorbed on the overlayer surface.

The XPS measurements in Figures 3 and S5 give a useful estimate of SiO<sub>x</sub>C<sub>y</sub> overlayer composition, but the calculated compositions are not necessarily representative of the overlayer bulk since the inelastic mean free path of photoelectrons passing through Si ( $\approx$ 2.0 nm) is substantially less than the average overlayer thickness. <sup>52</sup> Overlayer uniformity is especially important to consider for the "top-down" UVozone conversion process, where reactive oxygen species generated in the UV-ozone chamber first react with the top atomic layers of PDMS before subsequent conversion of the buried layers, which proceeds more slowly due to transport limitations.<sup>27</sup> Thus, to probe differences between the nearsurface concentration of the  $SiO_xC_y$  overlayers and the composition adjacent to the SiO<sub>x</sub>C<sub>y</sub> buried interface, angleresolved X-ray photoelectron spectroscopy (ARXPS) measurements were performed on one partially cured sample ( $t_{\text{cure}} = 30$ min) and one fully cured sample ( $t_{\text{cure}} = 120 \text{ min}$ ) at three different emission angles ( $\theta$ ): 10, 40, and 70°. The reported emission angles are given by the angle between the XPS analyzer cone and the surface normal of the sample, meaning that spectra recorded at  $\theta = 70^{\circ}$  are more representative of the near-surface composition and those recorded at  $\theta = 10^{\circ}$  better reflect the composition of the bulk. Multiplex ARXPS scans

were taken over the C 1s, O 1s, Si 2p, and Pt 4f regions, with Si 2p spectra shown in Figure 4 and full spectra along with composition analysis provided in Figures S7 and S8.

Si 2p spectra of the fully cured sample (Figure 4a) were fit with a single peak centered at 103.3 eV, closely matching the expected peak location for SiO<sub>2</sub>, and provided the best fit for all emission angles.<sup>53</sup> Importantly, the Si 2p spectra for the fully cured SiO<sub>x</sub>C<sub>y</sub> sample do not exhibit any significant changes in shape or position with varied emission angle, which implies that the 120 min SiO<sub>x</sub>C<sub>y</sub> overlayer is indeed "fully cured", with relatively uniform composition throughout the overlayer. Si 2p spectra for the partially cured sample (Figure 4b) were instead fit with two individual peaks, with the first peak centered at 103.7 eV associated with SiO<sub>2</sub> and the second peak centered at 102.4 eV to match the value for PDMS determined for the 0 min cure sample from Figure 3a. In contrast to the fully cured sample, the C 1s, Si 2p, and O 1s spectra of the partially cured overlayer exhibit clear shifts with  $\theta$ , indicating that the composition changes with depth. With increasing  $\theta$ , corresponding to increasing surface sensitivity, the Si 2p spectra exhibit increasing SiO<sub>2</sub> character as the lower binding energy peak associated with Si in PDMS diminishes. At the largest emission angle,  $\theta = 70^{\circ}$ , the Si 2p spectra in the partially cured sample look very similar to that of the fully cured sample, suggesting that SiO<sub>x</sub>C<sub>y</sub> overlayers at each cure time have similar composition at their outer surfaces. However, differences in the Si 2p spectra measured at  $\theta = 10^{\circ}$  show that the local binding environment of Si atoms located deeper within the overlayers is strongly dependent on cure time. For these partially cured overlayers, the transition between the SiO<sub>x</sub>-like surface and the PDMS-like interface appears to manifest as a gradual change in composition; however, it is also possible that this change could be abrupt, as would be the case if the ozone and oxygen radical species are highly reactive in the overlayer film and would not permeate any further until all reactive material closer to the surface is exhausted.

The surface chemistry of the  $SiO_xC_y$  overlayers was further interrogated by measuring water contact angles to quantify the hydrophobic character of the top surface of the overlayers. Contact angles are reported as the angle between the sample/droplet and droplet/air interfaces and are provided in Figure S3. The contact angle for the uncured PDMS MCECs was found to be  $108.9 \pm 1.1^\circ$ , similar to expected values for trimethyl siloxy-terminated PDMS. <sup>54</sup> The contact angle then

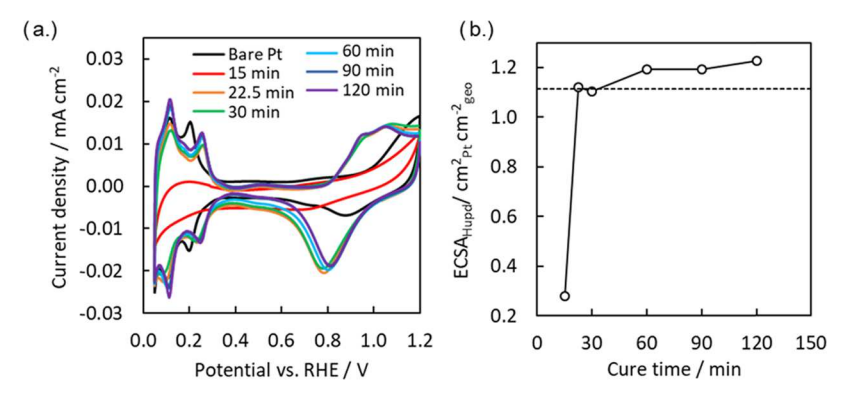


Figure 5. (a) CV curves of  $SiO_xC_y$  Pt electrodes of varying UV-ozone cure times taken in 0.5 M sulfuric acid for the 10th cycle of CV taken at a scan rate of 10 mV s<sup>-1</sup>. The bare Pt sample did not undergo any UV-ozone treatment. Electrochemically active surface area (ECSA) calculated using the integrated charge from the  $H_{upd}$  region (0.05–0.35 V vs RHE) in (a) normalized by the geometric area of the exposed electrode is presented in (b). The dashed line represents the ECSA for the bare Pt control.

decreases abruptly over the first 60 min of UV–ozone curing, reaching a final value of 37.9  $\pm$  1.8° after 120 min. This decrease in water contact angle, combined with XPS characterization, shows that the surface of SiO<sub>x</sub>C<sub>y</sub> overlayers becomes more hydrophilic as PDMS is converted to SiO<sub>x</sub> with increasing SiO<sub>2</sub> character and is consistent with previous studies that have reported the hydrophilic nature of most silica surfaces. <sup>55</sup>

**3.2. Electrochemical Characterization of the Buried Pt Interface of SiO**<sub>x</sub>C<sub>y</sub>**IPt Electrodes.** To better understand how the SiO<sub>x</sub>C<sub>y</sub> composition at the buried interface influences electrochemical characteristics of the underlying Pt thin film, cyclic voltammetry (CV) measurements were used to probe changes in the hydrogen underpotential deposition ( $H_{\rm upd}$ ) and platinum oxidation/reduction features, which have been extensively investigated for Pt electrocatalysts over the years. As the peak areas and peak center locations associated with these well-understood processes can indicate changes in electrochemically active surface area and proton binding energetics, their evaluation informs how the observed changes in overlayer composition and structure impact the local reaction environment at the buried interface. S9

The influence of SiO<sub>x</sub>C<sub>y</sub> overlayer composition on H<sub>upd</sub> and Pt oxide (PtO<sub>x</sub>) redox behaviors was evaluated by conducting CV in deaerated 0.5 M H<sub>2</sub>SO<sub>4</sub> (Figure S11). CV cycles initiated at potentials not sufficiently positive enough to induce electrochemical Pt oxidation reveal that the amount of PtO<sub>x</sub> species initially present at the buried interface varies with cure time where electrodes treated for the full 120 min show similar PtO<sub>x</sub> reduction signal to the bare Pt, and shorter cure electrodes demonstrate lower integrated reductive area, signifying that oxidative species formed during UV-ozone treatment oxidize more of the underlying Pt interface at longer cure times. The onset potential for these initial PtO<sub>x</sub> reduction peaks also shifts to lower potentials with decreasing cure time, meaning that the PtO<sub>x</sub> species formed on the shorter cure electrodes are less easily reduced electrochemically, as has been seen previously when altering the composition of the underlying Pt catalyst.<sup>22</sup> Such findings reveal that both the structure and energetics of the SiO<sub>x</sub>C<sub>y</sub>|Pt buried interface appear to be strongly dependent on the length of UV-ozone treatment.

Upon completion of the first CV scan segment, electrodes were cycled for 20 total cycles between 0.05 and 1.25 V vs RHE at 10 mV s $^{-1}$  to quantify the integrated  $H_{upd}$  signal.

Figure 5a contains the final cycle measured at 10 mV s<sup>-1</sup>, where H<sub>upd</sub> features associated with underpotential adsorption and desorption of H atoms are seen for all samples at potentials between the negative scan vertex and 0.3 V vs RHE. Sharp, distinct peaks coinciding with different Pt crystal facets appear for the bare Pt and 22.5–120 min SiO<sub>x</sub>C<sub>y</sub>|Pt electrodes. All samples except the 15 min cure time sample have comparable integrated H<sub>upd</sub> areas and thus exhibit similar ECSA with no significant differences in the number of active sites at their buried interfaces. From Figure 5b, the ECSA calculated for longer cure time samples actually exceeds that of the bare Pt electrode by ≈10%, perhaps caused by oxidationinduced roughening from the longer UV-ozone exposure for these samples.<sup>60</sup> Conversely, these results suggest that the 15 min cure time electrode has substantially lower ECSA than the other electrodes. Ellipsometry taken of the 15 min SiO<sub>x</sub>C<sub>y</sub>|Pt electrode following CV also revealed a large decrease (94%) in the overlayer thickness, meaning that the overlayer was largely removed during testing. Due to the lack of overlayer stability and substantial decrease in ECSA, samples treated for 15 min or less were omitted from all further electrochemical experiments.

Besides introducing changes to the  $H_{upd}$  features, the  $SiO_xC_y$ overlayers also caused significant changes in the CV features at positive potentials (0.6-1.2 V vs RHE) associated with the electrochemical oxidation and reduction of PtO<sub>x</sub> species. CV curves for all encapsulated electrodes with cure times  $\geq 22.5$ min show a negative shift in the onset for Pt oxidation by 50-100 mV and a much larger integrated Pt oxidation signal compared to the bare Pt electrodes. As previously suggested, we attribute the observed shift in the Pt oxidation onset potential to the ability of the SiO<sub>x</sub>C<sub>y</sub> overlayers to suppress the adsorption of sulfate anions, which are known to bond strongly to Pt surfaces and delay the Pt oxidation onset potential compared to that seen in supporting electrolytes with less strongly adsorbing species, such as perchloric acid. 56,61 Thus, the similar Pt oxidation onset potentials and integrated PtO<sub>x</sub> peak areas of the 30-120 min SiO<sub>x</sub>C<sub>v</sub>IPt electrodes imply that cure time does not significantly affect the ability of the  $SiO_xC_y$ overlayers to reject sulfate ions.

**3.3.** Controlling Proton and O<sub>2</sub> Fluxes through  $SiO_xC_y$  Overlayers. The influence of UV—ozone treatment on the transport properties of  $SiO_xC_y$  overlayers was investigated by measuring the transport-limited current densities of  $SiO_xC_y$ Pt electrodes for two commonly studied electrochemical reac-

tions: (i) the hydrogen evolution reaction (HER) and (ii) the oxygen reduction reaction (ORR), which are shown in eqs 1 and 2 for operation in an acidic environment along with their standard reduction potentials ( $E^{\circ}$ ). These two reactions were chosen for this study due to their importance for electrolysis and fuel cell applications while also involving redox species that are characterized by vastly different sizes, charge, and solubility limits

$$2H^+ + 2e^- \leftrightarrow H_2$$
;  $E^\circ = 0.0 \text{ V vs NHE}$  (1)

$$O_2 + 4H^+ + 4e^- \leftrightarrow 2H_2O; E^\circ = 1.23 \text{ V vs NHE}$$
 (2)

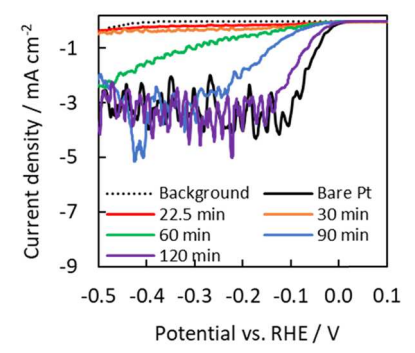
When the reaction rate is limited by the transport of reactant(s) to the electrocatalytic active sites through diffusion alone, the limiting current density  $(i_{lim})$  for a planar electrode operating at steady state is given by

$$i_{\text{lim}} = \frac{n \cdot F \cdot P_j}{s_j} \cdot \frac{C_j(x = \delta_0)}{t_0}$$
(3)

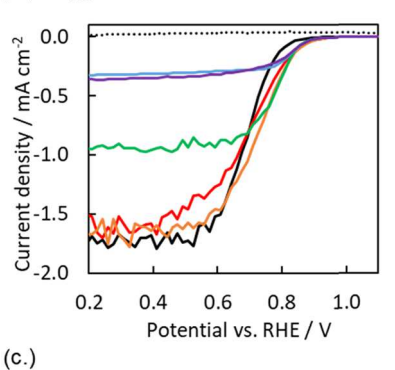
where n is the electron-transfer number, F is the Faraday constant,  $P_j$  is the permeability of species j,  $s_j$  is the stoichiometric coefficient of species j,  $t_o$  is the thickness of the overlayer, x is the distance from the overlayer/catalyst interface, and  $C_j(x=\delta_o)$  is the concentration of species j at the overlayer/electrolyte interface. Equation 3 assumes that convection and migration are negligible within the overlayer. For reactions for which there are two coreactants, the limiting species j is that which gives the smallest transport-limited flux across the overlayer. By knowing the bulk concentration of reactants, and measuring the resultant limiting current produced from these reactions, estimates for the permeabilities of protons and molecular  $O_2$  through  $SiO_xC_y$  overlayers of differing structure and composition can be obtained.

In this study, these limiting current densities for the HER and ORR were acquired by carrying out linear sweep voltammetry (LSV) or CV in acidic solutions containing dilute concentrations of the limiting reactant (H<sup>+</sup> or O<sub>2</sub>). Figure 6a contains the HER LSV curves, which were recorded in 5 mM H<sub>2</sub>SO<sub>4</sub> + 495 mM Na<sub>2</sub>SO<sub>4</sub> while sweeping the applied potential from 0.2 to −0.6 V vs RHE. The bare Pt electrode exhibits an HER onset potential close to 0.0 V vs RHE, reflecting the fast kinetics associated with proton reduction on Pt. At about -0.1 V vs RHE, the bare Pt electrode reaches an average limiting current density of -3.33 $\pm$  0.06 mA cm<sup>-2</sup> and sustains this value until the onset of water reduction at about -0.5 V vs RHE. The LSV curves for the longer cure time (90 and 120 min) SiO<sub>x</sub>C<sub>v</sub>IPt electrodes also show similar HER onset potentials and limiting current densities to those seen for bare Pt, although these samples require larger overpotentials to reach similar HER limited current densities. Even larger deviations in the LSV curves are observed for SiO<sub>x</sub>C<sub>y</sub>|Pt samples with cure times of 60 min or less. The LSV curve for the 60 min cure time sample shows an HER onset potential shifted slightly negative with respect to 0.0 V vs RHE, but the increase in reduction current is very gradual and a true limiting current is not reached before the onset of water reduction at more negative potentials. SiO<sub>x</sub>C<sub>v</sub>|Pt electrodes with the shortest cure times ( $t_{\text{cure}} = 30$  and 22.5 min) also show gradual growth compared to the unencapsulated or fully cured samples before reaching limiting current densities that are 0.21 and 0.35 mA  $\,\mathrm{cm}^{-2}$  larger than the background current for the same samples (Figure S12). As

## (a.) Hydrogen Evolution Reaction



# (b.) Oxygen Reduction Reaction



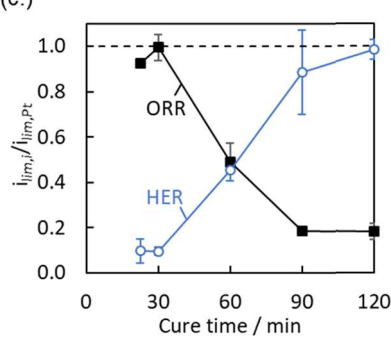


**Figure 6.** Mass transport limiting currents for  $SiO_xC_y|Pt$  samples of varying treatment times under constant hydrodynamic conditions in a stirred electrolyte for (a) hydrogen evolution in 5 mM  $H_2SO_4 + 495$  mM  $Na_2SO_4$  and (b) oxygen reduction in  $O_2$ -saturated 500 mM  $H_2SO_4$ . Data for all LSVs is presented as a five-point average to reduce noise. Dotted lines denote a bare Pt electrode in the absence of protons (in pH 7 500 mM  $Na_2SO_4$ ) or oxygen ( $N_2$  sat. 500 mM sulfuric acid). Trends in limiting current densities for HER and ORR as a function of  $SiO_xC_y$  cure time are summarized in (c), where the limiting current density ( $i_{lim}$ ) for each sample has been normalized by the limiting current for a bare Pt sample ( $i_{lim,Pt}$ ) recorded under the identical testing conditions. Error bars represent the standard deviation taken for two to three identical measurements.

detailed in Section SIV of the SI, H<sup>+</sup> permeabilities ( $P_{\rm H}^+$ ) through SiO $_x$ C $_y$  overlayers can be estimated from the HER limiting current densities for the bare Pt and SiO $_x$ C $_y$ lPt electrodes so long as the value of the latter is less than the former.  $P_{\rm H}^+$  was estimated to be  $(5.2 \pm 1.6) \times 10^{-10}$  and  $(1.0 \pm 0.5) \times 10^{-7}$  cm $^2$  s $^{-1}$  for a 30 and 120 min sample, respectively. The larger value is much greater than the proton permeabilities previously reported for SiO $_x$  overlayers deposited on 3 nm thick Pt substrates, <sup>15</sup> for which the underlying titanium adhesion layer has been shown to impact the structure and transport properties of the SiO $_x$  overlayers. <sup>22</sup>

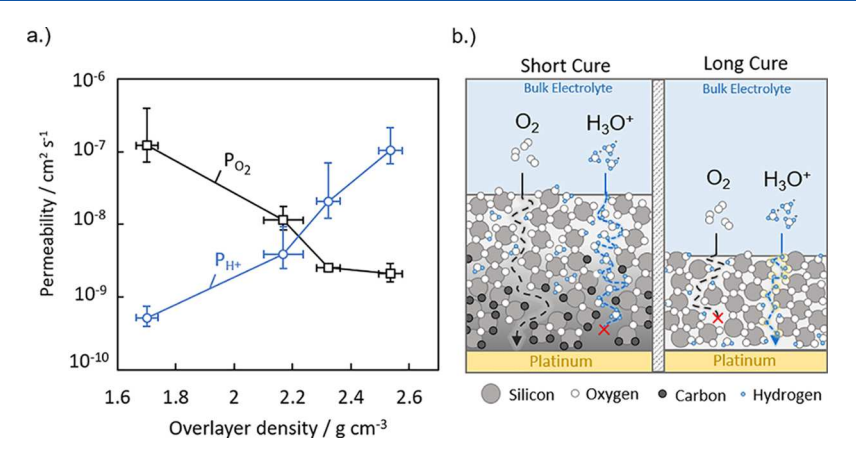


Figure 7. (a)  $O_2$  and  $H^+$  permeabilities calculated from limiting currents for oxygen reduction in 500 mM  $H_2SO_4$  and proton reduction in 5 mM  $H_2SO_4$  + 495 mM  $Na_2SO_4$ , respectively, plotted as a function of  $SiO_xC_y$  overlayer density. (b) Schematic representations showing possible transport mechanisms for  $O_2$  and  $H^+$  in  $SiO_xC_y$  overlayers with short (left image) and long (right image) cure times.

For samples with  $t_{\text{cure}} \leq 30$  min, a potential-independent limiting current is never seen, which may suggest the presence of electromigration effects. The same monotonic trend between HER current density and cure time also appears during chronoamperometry measurements at -0.1 V vs RHE in the same electrolyte (Figure S13), showing that the different proton fluxes viewed in the LSV measurements in Figure 6a can be sustained under potentiostatic measurements as well. Such a result highlights the ability to use overlayer composition and structure to control proton flux to an electrocatalytic buried interface where the local pH is considerably higher than that in the acidic electrolyte. Following all electrochemical experiments, the thicknesses of  $SiO_xC_y$  overlayers were measured by ellipsometry to assess overlayer stability and revealed no significant losses of overlayer thickness following HER in 5 mM sulfuric acid.

To probe  $O_2$  transport through the  $SiO_xC_y$  overlayers, the ORR performance of SiO<sub>x</sub>C<sub>y</sub>|Pt electrodes was measured by recording CVs in an O2-saturated 0.5 M H2SO4 electrolyte (Figure 6b). Under these acidic conditions, the bulk concentration of H<sup>+</sup> is  $\approx$ 2000 times greater than the solubility limit of O<sub>2</sub>, ensuring that the ORR is limited by the transport of O2 rather than H+. For a bare Pt electrode, the ORR onset potential is ≈0.9 V vs RHE before reaching a limiting current density of -1.72 mA cm<sup>-2</sup>. The limiting current densities of the 22.5 and 30 min SiO<sub>x</sub>C<sub>v</sub>IPt electrodes are only slightly less than that recorded for bare Pt, but the limiting current density decreases by up to 82% for electrodes with cure times ≥90 min. ORR measurements were also carried out in an O2saturated 0.1 mM H<sub>2</sub>SO<sub>4</sub> + 499.9 Na<sub>2</sub>SO<sub>4</sub> electrolyte (Figure S14), showing that shorter cure time  $SiO_xC_y|Pt$  electrodes can reduce O2 through a H2O-mediated mechanism at such low bulk proton concentrations. In contrast, the high  $P_{H^+}$ ,  $O_{2^-}$ blocking 120 min cure time SiO<sub>x</sub>C<sub>y</sub>IPt electrodes maintain a H<sup>+</sup>-mediated ORR mechanism over the full range of potentials tested, demonstrating that changes to the overlayer composition can completely change the reaction mechanism at the buried interface through variation in the local concentration of reactants at the buried interface microenvironment. Following the same procedure as was used for estimating  $P_{H^+}$ , oxygen permeability  $(P_{O_2})$  values were computed from the ORR limiting currents in Figure 6b and found to range between (1.2  $\pm 0.8$ )  $\times 10^{-7}$  and  $(2.1 \pm 0.6 \times 10^{-9})$  cm<sup>2</sup> s<sup>-1</sup> for the 30 and 120 min cure time  $SiO_xC_y|Pt$  electrodes, respectively.

Permeability values for the full set of samples are presented in Table S1 of the SI. Following ORR experiments, the thicknesses of  $SiO_xC_y$  overlayers were measured by ellipsometry to assess overlayer stability, revealing no significant decrease in measured thickness.

To summarize the results from the HER and ORR experiments, average limiting current densities were normalized by the average limiting current for bare Pt and plotted as a function of cure time (Figure 6c). This figure clearly shows the opposing effects that UV—ozone cure time has on the transport of H<sup>+</sup> and O<sub>2</sub> through  $\mathrm{SiO}_x\mathrm{C}_y$  overlayers, with increasing cure time correlating positively for the HER limiting current and negatively the ORR limiting current. For both cases, the most significant changes in transport behavior appear to occur when the cure time is increased from 30 to 90 min, which corresponds with the most significant changes in the structural and compositional characteristics of the overlayer presented in Section 3.1.

**3.4. Discussion.** The results presented in the previous sections demonstrate the dramatic impact that cure time has on the structural and electrochemical characteristics of  $\mathrm{SiO}_x \mathrm{C}_y$ . Pt electrodes. ATR-FTIR, XPS, and ellipsometry measurements revealed that  $\mathrm{SiO}_x \mathrm{C}_y$  overlayers become more dense, homogeneous, and carbon-deficient as cure time increases. Shorter cure times (<60 min) produce  $\mathrm{SiO}_x \mathrm{C}_y$  overlayers characterized by gradient compositions with  $\mathrm{SiO}_2$ -like character at the outer surface and PDMS-like character at the buried  $\mathrm{SiO}_x \mathrm{C}_y \mathrm{IP}_1$  interface. Despite these differences in composition at the buried interface, CV measurements revealed that there is minimal loss in the electrochemically active surface area for all electrodes with  $t_{\mathrm{cure}} \geq 22.5$  min.

Importantly, Figure 6 shows that the structural and compositional characteristics of the  $\mathrm{SiO}_x\mathrm{C}_y$  overlayers are strongly correlated with proton and  $\mathrm{O}_2$  permeabilities, which increase and decrease with increasing cure time, respectively. The trend of decreasing  $\mathrm{O}_2$  permeability with increasing cure time and overlayer density is well supported by studies of silicon oxide-based gas diffusion membranes. For both PDMS and  $\mathrm{SiO}_2$  membranes explored in those studies, the chemical interactions between  $\mathrm{O}_2$  and the membrane are weak so that diffusion proceeds primarily through the available free volume in the membrane, resulting in  $\mathrm{O}_2$  transport behavior that is best described by a solution diffusion model. Thus, the density and associated free volume of the  $\mathrm{SiO}_x\mathrm{C}_y$  overlayer

strongly influence the diffusivity of O2, consistent with the inverse relationship between PO, and overlayer density shown in Figure 7a. It follows that the substantial decrease in the ORR limiting current seen for denser 90-120 min SiO, C, Pt electrodes likely results from decreasing the average size of the available free volume elements within the overlayer below a critical value necessary to enable facile O2 diffusion. This explanation is depicted on the left side of Figure 7b, which shows O2 diffusing through large free volume elements in the less dense overlayer. This picture is contrasted on the right side of Figure 7b by a denser SiO<sub>x</sub>C<sub>y</sub> overlayer obtained at longer cure time, for which the compressed material offers few continuous pathways for O2 diffusion. Consistent with this description, other researchers have shown that dense SiO<sub>2</sub> overlayers deposited onto Pt thin films using atomic layer deposition (ALD) or photodeposition methods completely block detectable ORR signal. 24,64 In addition to these structural influences, the increasingly hydrophilic nature of SiO<sub>x</sub>C<sub>y</sub> overlayers subjected to longer cure times can be expected to weaken the overlayer-oxygen interactions, resulting in a decrease in the solubility of oxygen within the overlayer that further diminishes  $P_{O}$ ,  $^{23,65}$ 

Unlike  $O_2$ ,  $H^+$  is known to transport through silica by a facilitated transport or Grotthuss-type mechanism.  $^{32,66,67}$  This transport mechanism is made possible by the ability of Si–O moieties to react with protons to form bridging hydroxyl (BOH) groups.  $^{68-71}$  If there is a continuous matrix of  $SiO_x$  with a sufficiently high density of these sites, a hydrogenbonding network is formed within which protons can "hop" between adjacent BOH groups in a manner that is similar to the transfer of protons along the hydrogen-bonding network in water.  $^{66,70-73}$  Because BOH groups within  $SiO_xC_y$  overlayers are believed to serve as fixed nodes that shuttle protons across the nanomembrane, disruptions or discontinuities in the  $SiO_x$  matrix that contains these groups can be expected to greatly reduce  $H^+$  permeability.

For membranes that rely on facilitated transport mechanisms, a key parameter for determining species permeability is the free carrier distance (l), defined as the equilibrium distance between two reactive carrier centers.<sup>74</sup> Thus, increasing the average distance between Si and O groups that can form reactive BOH bridges beyond the maximum allowable hopping distance for a proton is expected to disrupt the hydrogenbonding network and significantly impede proton transport. We postulate that this is what occurs when the UV-ozone cure time applied to  $SiO_xC_y$  overlayers is too short. This is supported by the FTIR and ARXPS measurements from this study, which showed that the partially cured 30 min SiO<sub>x</sub>C<sub>y</sub> overlayers still retain PDMS-like character, especially at the SiO<sub>x</sub>C<sub>v</sub>|Pt buried interface. Given that unmodified PDMS has poor proton solubility and conductivity, 75 this PDMS-like bottom layer that contains a higher concentration of methylcoordinated Si groups, and thus a lower concentration of potential Si carriers, likely obstructs the H-bond network of the overlayer that separates the catalytic buried interface from the bulk electrolyte. Conversely, the presence of intense LO phonon peaks in the FTIR spectra of SiO<sub>x</sub>C<sub>v</sub>IPt electrodes subjected to longer cure times gives direct evidence of longrange order of a Si-O bond network, and the uniform Si 2p spectra in ARXPS measurements indicate that this SiO<sub>x</sub> network extends across the entire overlayer thickness. Furthermore, longer cure times were shown to increase the

density of the overlayer, which effectively decreases the average hopping distance between neighboring Si—O groups. As detailed in Section SIII of the SI, the average nearest-neighbor distances between oxygen-coordinated Si atoms  $(l_{\rm Si-Si})$  were estimated based on overlayer densities and compositions calculated from XPS. As shown in Figure S9, proton permeabilities only reach appreciable values for  $l_{\rm Si-Si}$  values less than 5 Å. This observation is in excellent agreement with the computed maximum proton hopping distance between adjacent carriers presented by Godet and Pasquarello,  $^{66}$  thus providing further evidence that proton transport through ultrathin SiO $_x$  overlayers occurs through a facilitated transport mechanism.

Analyzing trends in the HER and ORR limiting current densities for the SiO<sub>x</sub>C<sub>y</sub>IPt electrodes of various cure times reveals distinct differences in how reactant species can diffuse through these overlayers, demonstrating the potential to control the relative fluxes of protonic and molecular species to the electrocatalytic buried interface of an MCEC. For membranes that separate species on the basis of their size, there is a common trade-off between permeability  $(P_i)$  and selectivity  $(P_i/P_i)$  that places an "upper bound" on membrane performance. This so-called Robeson limit has been extensively studied for gas diffusion membranes, 76,77 with similar relationships observed for liquid separation membranes as well.<sup>78</sup> It describes the trade-off between permeability and selectivity on the basis of the relative sizes and solubilities of the two diffusing species of interest, as well as their size relative to the free volume elements through which they diffuse. 77,79 Thus, for two species with similar size that diffuse exclusively in the available free volume of the membrane material, it is very difficult to increase selectivity toward the smaller species without significantly compromising permeability. However, since proton transport in the  $SiO_xC_y$  overlayers does not rely predominantly on free volume diffusion, this work demonstrates a rare example where selectivity and permeability are not limited by this trade-off. Of the few examples where membranes break the Robeson limit,  $^{80-82}$  functionalized groups dispersed in the membrane are employed to shuttle the desired permeant species using a facilitated transport mechanism, just as we have proposed for the  $SiO_x$  overlayers in this presented study.

The ability of ultrathin coatings to break the Robeson limit for electrochemical systems requiring proton coreactants could have important implications for a wide range of electrochemical applications involving proton transfer and/or protoncoupled electron-transfer reactions. A proton is a necessary coreactant for a number of electrochemical reactions for which it is desirable to maximize or minimize proton flux or to achieve specific intermediate proton fluxes that enable an optimal pH or coverage of adsorbed H at the electrocatalytic buried interface. For example, controlling the relative fluxes of H<sup>+</sup> and O<sub>2</sub> is attractive for membraneless electrolysis cells where it may be advantageous to maximize proton transport for efficient HER at the cathode while blocking the undesirable reduction of O<sub>2</sub>. 83,84 For other reactions, suppressing, but not eliminating, proton or O<sub>2</sub> fluxes may be beneficial. In the ORR and OER occurring in acidic or pH-neutral environments, it is desirable to engineer coatings that maximize permeability for O2 while still maintaining sufficient proton permeability to ensure that low proton fluxes do not limit the overall reaction rate or lead to extreme pH at the buried interface. Similarly, intermediate or low proton fluxes may be beneficial in other

electrochemical reactions such as  $CO_2$  reduction, where high concentrations of protons in the electrolyte lead to undesirable HER and low faradic efficiency for the desired reaction. Res, 85, 86 However, completely minimizing the hydrogen-bonding interactions of the overlayer may not be entirely beneficial for these applications, as water or protons are still required coreactants for  $CO_2$  reduction. Thus, tailoring overlayer composition to limit the HER while still maintaining a minimum concentration of coreacting protons could provide a balance that optimizes the faradic efficiency toward  $CO_2$  reduction. In a wide range of applications, overlayers that enhance the transport of protons and/or other small molecules while suppressing the permeability of larger impurity species can also improve electrocatalyst durability through poison resistance.

To expand the use of MCECs to other electrochemical systems, future research efforts aimed at tuning overlayer composition and structure would benefit from studies that explore larger numbers of reactant species with varying charge, polarity, and/or size for different membrane compositions. Such investigations are expected to lead to more general design rules for overlayers that can be broadly applied across numerous classes of reactions and operating conditions. Further research efforts incorporating in situ characterization and/or atomistic modeling of species transport are also needed to support ex situ observations such as those carried out through this study and could provide a better understanding of the local conditions of the buried interface microenvironment where the reaction occurs. Though many fundamental questions remain about transport and catalysis in MCECs, these architectures represent a promising opportunity to finetune electrocatalyst properties for a wide range of complex reaction systems in ways that are not possible with conventional electrocatalysts.

# 4. CONCLUSIONS

Results from this study illustrate both the opportunities and challenges associated with designing MCECs with tunable overlayer composition and structure that can be used to control fluxes of protons and oxygen to electrocatalytic buried interfaces. By varying the cure time of carbon-modified silicon oxide (SiO<sub>x</sub>C<sub>y</sub>) overlayers fabricated using a room-temperature UV-ozone process, this work demonstrated the ability to precisely tune several overlayer characteristics, including thickness, carbon content, density, and hydrophobicity. These characteristics were found to strongly influence the fluxes of H<sup>+</sup> and O<sub>2</sub> to active sites, as probed through the hydrogen evolution and oxygen reduction reactions, respectively. Moreover, opposing trends in H<sup>+</sup> and O<sub>2</sub> permeabilities were observed as a function of overlayer cure times. H+ transport was enhanced at longer cure times, which promotes the formation of a dense, uniform overlayer containing a continuous SiO<sub>x</sub> network that is well suited for promoting H<sup>+</sup> hopping along Si-O moieties through a facilitated transport mechanism. In contrast, oxygen permeability was largest for SiO<sub>x</sub>C<sub>y</sub> overlayers exposed to shorter cure times, which were characterized by lower densities that can promote O<sub>2</sub> diffusion through larger free volume elements. As a result of these opposite transport trends, transport of one species can be favored over the other without sacrificing overall species flux to electrocatalytic active sites. This functionality of semipermeable overlayers to tailor the relative fluxes of reactant species is expected to present unique opportunities for MCECs to

improve electrocatalyst performance for a wide range of electrochemical reactions.

## ASSOCIATED CONTENT

# Supporting Information

The Supporting Information is available free of charge at https://pubs.acs.org/doi/10.1021/acsaem.0c02359.

Physical characterization of  $SiO_xC_y|Pt$  electrodes (Section SI); X-ray photoelectron spectroscopy (XPS) characterization (Section SII); description of overlayer density calculations (Section SIII); description of permeability calculations (Section SIV); supporting electrochemical measurements (Section SV); and references (Section SVI) (PDF)

## AUTHOR INFORMATION

# **Corresponding Author**

Daniel V. Esposito — Department of Chemical Engineering, Columbia Electrochemical Energy Center, Lenfest Center for Sustainable Energy, Columbia University in the City of New York, New York, New York 10027, United States;

orcid.org/0000-0002-0550-801X; Phone: 212-854-2648; Email: de2300@columbia.edu

## **Authors**

Marissa E. S. Beatty — Department of Chemical Engineering, Columbia Electrochemical Energy Center, Lenfest Center for Sustainable Energy, Columbia University in the City of New York, New York, New York 10027, United States

Eleanor I. Gillette – Department of Chemistry and Biochemistry, University of San Diego, San Diego, California 92110-2492, United States

Alexis T. Haley – Department of Chemical Engineering, Columbia Electrochemical Energy Center, Lenfest Center for Sustainable Energy, Columbia University in the City of New York, New York, New York 10027, United States

Complete contact information is available at: https://pubs.acs.org/10.1021/acsaem.0c02359

#### Notes

The authors declare no competing financial interest.

## ACKNOWLEDGMENTS

We acknowledge the Columbia University Columbia Nano Initiative clean room facility for the use of the physical vapor deposition and the Shared Materials Characterization Laboratory for the use of AFM, ellipsometer, and XPS. We would also like to acknowledge Dr. Ngai Yin Yip for providing facilities for contact angle measurements as well as valuable discussion and feedback. E.I.G. also acknowledges financial support from the University of San Diego. This material is based upon work supported by the National Science Foundation under grant number CBET-1752340. Any opinions, findings, and conclusions or recommendations expressed in this material are those of the author(s) and do not necessarily reflect the views of the National Science Foundation.

# REFERENCES

(1) Wu, J.; Yuan, X. Z.; Martin, J. J.; Wang, H.; Zhang, J.; Shen, J.; Wu, S.; Merida, W. A Review of PEM Fuel Cell Durability:

- Degradation Mechanisms and Mitigation Strategies. J. Power Sources 2008, 184, 104–119.
- (2) Greeley, J.; Markovic, N. M. The Road from Animal Electricity to Green Energy: Combining Experiment and Theory in Electrocatalysis. *Energy Environ. Sci.* **2012**, *5*, 9246–9256.
- (3) Takenaka, S.; Hirata, A.; Tanabe, E.; Matsune, H.; Kishida, M. Preparation of Supported Pt-Co Alloy Nanoparticle Catalysts for the Oxygen Reduction Reaction by Coverage with Silica. *J. Catal.* **2010**, 274, 228–238.
- (4) Wang, Y. J.; Zhao, N.; Fang, B.; Li, H.; Bi, X. T.; Wang, H. Carbon-Supported Pt-Based Alloy Electrocatalysts for the Oxygen Reduction Reaction in Polymer Electrolyte Membrane Fuel Cells: Particle Size, Shape, and Composition Manipulation and Their Impact to Activity. *Chem. Rev.* **2015**, *115*, 3433–3467.
- (5) Liu, Z.; Ma, L.; Zhang, J.; Hongsirikarn, K.; Goodwin, J. G. Pt Alloy Electrocatalysts for Proton Exchange Membrane Fuel Cells: A Review. *Catal. Rev.* **2013**, *55*, 255–288.
- (6) Kang, Y.; Yang, P.; Markovic, N. M.; Stamenkovic, V. R. Shaping Electrocatalysis through Tailored Nanomaterials. *Nano Today* **2016**, *11*, 587–600.
- (7) Trogadas, P.; Ramani, V.; Strasser, P.; Fuller, T. F.; Coppens, M. O. Hierarchically Structured Nanomaterials for Electrochemical Energy Conversion. *Angew. Chem., Int. Ed.* **2016**, *55*, 122–148.
- (8) Mukerjee, S. Particle Size and Structural Effects in Platinum Electrocatalysis. *J. Appl. Electrochem.* **1990**, *20*, 537–548.
- (9) Sharma, S.; Pollet, B. G. Support Materials for PEMFC and DMFC Electrocatalysts A Review. *J. Power Sources* **2012**, 208, 96–119
- (10) Man, I. C.; Su, H. Y.; Calle-Vallejo, F.; Hansen, H. A.; Martínez, J. I.; Inoglu, N. G.; Kitchin, J.; Jaramillo, T. F.; Nørskov, J. K.; Rossmeisl, J. Universality in Oxygen Evolution Electrocatalysis on Oxide Surfaces. *ChemCatChem* **2011**, *3*, 1159–1165.
- (11) Govindarajan, N.; Koper, M. T. M.; Meijer, E. J.; Calle-Vallejo, F. Outlining the Scaling-Based and Scaling-Free Optimization of Electrocatalysts. *ACS Catal.* **2019**, *9*, 4218–4225.
- (12) Esposito, D. V. Membrane Coated Electrocatalysts—an Alternative Approach to Achieving Stable and Tunable Electrocatalysis. *ACS Catal.* **2018**, *8*, 457–465.
- (13) Takenaka, S.; Miyamoto, H.; Utsunomiya, Y.; Matsune, H.; Kishida, M. Catalytic Activity of Highly Durable Pt/CNT Catalysts Covered with Hydrophobic Silica Layers for the Oxygen Reduction Reaction in PEFCs. J. Phys. Chem. C 2014, 118, 774–783.
- (14) Joo, S. H.; Park, J. Y.; Tsung, C. K.; Yamada, Y.; Yang, P.; Somorjai, G. A. Thermally Stable Pt/Mesoporous Silica Core-Shell Nanocatalysts for High-Temperature Reactions. *Nat. Mater.* **2009**, *8*, 126–131.
- (15) Labrador, N. Y.; Songcuan, E. L.; De Silva, C.; Chen, H.; Kurdziel, S. J.; Ramachandran, R. K.; Detavernier, C.; Esposito, D. V. Hydrogen Evolution at the Buried Interface between Pt Thin Films and Silicon Oxide Nanomembranes. ACS Catal. 2018, 8, 1767–1778.
- (16) Audichon, T.; Napporn, T. W.; Canaff, C.; Morais, C.; Comminges, C.; Kokoh, K. B. IrO2 Coated on RuO2 as Efficient and Stable Electroactive Nanocatalysts for Electrochemical Water Splitting. *J. Phys. Chem. C* **2016**, *120*, 2562–2573.
- (17) Robinson, J. E.; Labrador, N. Y.; Chen, H.; Sartor, B. E.; Esposito, D. V. Silicon Oxide-Encapsulated Platinum Thin Films as Highly Active Electrocatalysts for Carbon Monoxide and Methanol Oxidation. ACS Catal. 2018, 8, 11423–11434.
- (18) Maeda, K.; Teramura, K.; Lu, D.; Saito, N.; Inoue, Y.; Domen, K. Noble-Metal/Cr2O3 Core/Shell Nanoparticles as a Cocatalyst for Photocatalytic Overall Water Splitting. *Angew. Chem., Int. Ed.* **2006**, 45, 7806–7809.
- (19) Vos, J. G.; Wezendonk, T. A.; Jeremiasse, A. W.; Koper, M. T. M. MnOx/IrOx as Selective Oxygen Evolution Electrocatalyst in Acidic Chloride Solution. *J. Am. Chem. Soc.* **2018**, *140*, 10270–10281.
- (20) Liu, Y.; Leung, K. Y.; Michaud, S. E.; Soucy, T. L.; McCrory, C. C. L. Controlled Substrate Transport to Electrocatalyst Active Sites for Enhanced Selectivity in the Carbon Dioxide Reduction Reaction. *Comments Inorg. Chem.* **2019**, *39*, 242–269.

- (21) Labrador, N. Y.; Li, X.; Liu, Y.; Tan, H.; Wang, R.; Koberstein, J. T.; Moffat, T. P.; Esposito, D. V. Enhanced Performance of Si MIS Photocathodes Containing Oxide-Coated Nanoparticle Electrocatalysts. *Nano Lett.* **2016**, *16*, 6452–6459.
- (22) Beatty, M. E. S.; Chen, H.; Labrador, N. Y.; Lee, B. J.; Esposito, D. V. Structure-Property Relationships Describing the Buried Interface between Silicon Oxide Overlayers and Electrocatalytic Platinum Thin Films. *J. Mater. Chem. A* **2018**, *6*, 22287–22300.
- (23) Takenaka, S.; Miyazaki, T.; Matsune, H.; Kishida, M. Highly Active and Durable Silica-Coated Pt Cathode Catalysts for Polymer Electrolyte Fuel Cells: Control of Micropore Structures in Silica Layers. Catal. Sci. Technol. 2015, 5, 1133–1142.
- (24) Jo, W. J.; Katsoukis, G.; Frei, H. Ultrathin Amorphous Silica Membrane Enhances Proton Transfer across Solid-to-Solid Interfaces of Stacked Metal Oxide Nanolayers While Blocking Oxygen. *Adv. Funct. Mater.* **2020**, *30*, No. 1909262.
- (25) Pourbaix, M. Atlas of Electrochemical Equilibria in Aqueous Solutions, 1st ed.; National Association of Corrosion Engineers: Houston, 1974.
- (26) Mirley, C. L.; Koberstein, J. T. A Room Temperature Method for the Preparation of Ultrathin SiOx Films from Langmuir-Blodgett Layers. *Langmuir* **1995**, *11*, 1049–1052.
- (27) Ouyang, M.; Yuan, C.; Muisener, R. J.; Boulares, A.; Koberstein, J. T. Conversion of Some Siloxane Polymers to Silicon Oxide by UV/Ozone Photochemical Processes. *Chem. Mater.* **2000**, 12, 1591–1596.
- (28) Markov, D. A.; Lillie, E. M.; Garbett, S. P.; McCawle, L. J. Variation in Diffusion of Gases through PDMS Due to Plasma Surface Treatment and Storage Conditions. *Biomed. Microdevices* **2014**, *16*, 91–96.
- (29) Ouyang, M.; Klemchuk, P. P.; Koberstein, J. T. Exploring the Effectiveness of SiOx Coatings in Protecting Polymers against Photo-Oxidation. *Polym. Degrad. Stab.* **2000**, *70*, 217–228.
- (30) Fu, Y. J.; Qui, H. Z.; Liao, K. S.; Lue, S. J.; Hu, C. C.; Lee, K. R.; Lai, J. Y. Effect of UV-Ozone Treatment on Poly-(Dimethylsiloxane) Membranes: Surface Characterization and Gas Separation Performance. *Langmuir* **2010**, *26*, 4392–4399.
- (31) Chouler, J.; Bentley, I.; Vaz, F.; O'Fee, A.; Cameron, P. J.; Di Lorenzo, M. Exploring the Use of Cost-Effective Membrane Materials for Microbial Fuel Cell Based Sensors. *Electrochim. Acta* **2017**, 231, 319–326.
- (32) Nuccio, L. Diffusion of Small Molecules in Amorphous SiO<sub>2</sub>: Effects on the Properties of the Material and on Its Point Defects. Ph.D. Thesis, Dipartimento di Scienze Fisiche e Astronomiche, 2009.
- (33) Herz, H. G.; Kreuer, K. D.; Maier, J.; Scharfenberger, G.; Schuster, M. F. H.; Meyer, W. H. New Fully Polymeric Proton Solvents with High Proton Mobility. *Electrochim. Acta* **2003**, 48, 2165–2171.
- (34) Granados-Focil, S.; Woudenberg, R. C.; Yavuzcetin, O.; Tuominen, M. T.; Coughlin, E. B. Water-Free Proton-Conducting Polysiloxanes: A Study on the Effect of Heterocycle Structure. *Macromolecules* **2007**, *40*, 8708–8713.
- (35) Kischkat, J.; Peters, S.; Gruska, B.; Semtsiv, M.; Chashnikova, M.; Klinkmüller, M.; Fedosenko, O.; MacHulik, S.; Aleksandrova, A.; Monastyrskyi, G.; Flores, Y.; Masselink, W. T. Mid-Infrared Optical Properties of Thin Films of Aluminum Oxide, Titanium Dioxide, Silicon Dioxide, Aluminum Nitride, and Silicon Nitride. *Appl. Opt.* **2012**, *51*, 6789–6798.
- (36) Roychowdhury, T.; Cushman, C. V.; Synowicki, R. A.; Linford, M. R. Polydimethylsiloxane: Optical Properties from 191 to 1688 Nm (0.735–6.491 EV) of the Liquid Material by Spectroscopic Ellipsometry. *Surf. Sci. Spectra* **2018**, *25*, No. 026001.
- (37) Moulder, J. F.; Stickle, W. F.; Sobol, P. E.; Bomben, K. D. In *Handbook of X-ray Photoelectron Spectroscopy*; Chastain, J.; King, R. C., Eds.; Physical Electronics, Inc.: Eden Prairie, MN, 1995.
- (38) Wagner, C. D.; Davis, L. E.; Zeller, M. V.; Taylor, J. A.; Raymond, R. H.; Gale, L. H. Empirical Atomic Sensitivity Factors for Quantitative Analysis by Electron Spectroscopy for Chemical Analysis. *Surf. Interface Anal.* **1981**, *3*, 211–225.

- (39) Green, C. L.; Kucernak, A. Determination of the Platinum and Ruthenium Surface Areas in Platinum-Ruthenium Alloy Electrocatalysts by Underpotential Deposition of Copper. I. Unsupported Catalysts. J. Phys. Chem. B 2002, 106, 1036–1047.
- (40) Kuo, A. C. Poly(dimethylsiloxane). *Polymer Data Handbook*; Oxford University Press, 1999; pp 412–435.
- (41) Brückner, R. Properties and Structure of Vitreous Silica. I. J. Non-Cryst. Solids 1970, 5, 123-175.
- (42) Anthony, J. W.; Bideaux, R. A.; Bladh, K. W.; Nichols, M. C. Quartz. *Handbook of Mineralogy. III (Halides, Hydroxides, Oxides)*; Mineral Data Publishing, 1997; Vol. 3, pp 1967–1968.
- (43) Kuo, A. C. M. Polydimethylsiloxane. *Polymer Data Handbook*; Oxford University Press, 1999; pp 411–435.
- (44) Mirley, C. L.; Koberstein, J. T. A Room Temperature Method for the Preparation of Ultrathin SiOx Films from Langmuir-Blodgett Layers. *Langmuir* 1995, 11, 1049–1052.
- (45) Reusch, W. Virtual Textbook of Organic Chemistry; Michigan State University, 1999.
- (46) Tran, T. H.; Au, D. B.; Diawara, B.; Fatyeyeva, K.; Marais, S.; Ortiz, J.; Debarnot, D.; Poncin-Epaillard, F. How the Chemical Structure of the Plasma-Deposited SiOx Film Modifies Its Stability and Barrier Properties: FTIR Study. *Prog. Org. Coat.* **2019**, *137*, No. 105332.
- (47) Olsen, J. E.; Shimura, F. Infrared Reflection Spectroscopy of the SiO2-Silicon Interface. *J. Appl. Phys.* **1989**, *66*, 1353–1358.
- (48) Queeney, K. T.; Herbots, N.; Shaw, J. M.; Atluri, V.; Chabal, Y. J. Infrared Spectroscopic Analysis of an Ordered Si/SiO2 Interface. *Appl. Phys. Lett.* **2004**, *84*, 493–495.
- (49) Mundry, T.; Surmann, P.; Schurreit, T. Surface Characterization of Polydimethylsiloxane Treated Pharmaceutical Glass Containers by X-Ray-Excited Photo- and Auger Electron Spectroscopy. Fresenius' J. Anal. Chem. 2000, 368, 820–831.
- (50) Alfonsetti, R.; Lozzi, L.; Passacantando, P.; Picozzi, P.; Santucci, S. XPS Studies on SiOx Thin Films. *Appl. Surf. Sci.* **1993**, 70–71, 222–225.
- (51) Pesaran, A. A. In *Degradation of Desiccants upon Contamination*. *An Experimental Study*, ASME-JSES-JSME International Solar Energy Conference, 1991; pp 571–580.
- (52) Seah, M. P.; Dench, W. A. Quantitative Electron Spectroscopy of Surfaces. Surf. Interface Anal. 1979, 1, 2–11.
- (53) Alfonsetti, R.; Lozzi, L.; Passacantando, M.; Picozzi, P.; Santucci, S. XPS Studies on SiOx Thin Films. *Appl. Surf. Sci.* **1993**, 70–71, 222–225.
- (54) Pelayo, J. C.; Badiola, R. A.; Castanãres, J.; Pili, U.; Violanda, R.; Bacabac, R. Surface Geometry Based Hydrophobicity of the PDMS for Microfluidic Devices. *IOP Conf. Ser.: Mater. Sci. Eng.* **2015**, 79, No. 012027.
- (55) Ouyang, M.; Muisener, R. J.; Boulares, A.; Koberstein, J. T. UV-Ozone Induced Growth of a SiO(x) Surface Layer on a Cross-Linked Polysiloxane Film: Characterization and Gas Separation Properties. *J. Membr. Sci.* **2000**, *177*, 177–187.
- (56) Conway, B. E. Electrochemical At Noble Metals Oxide Film Formation As a Surface-Chemical Process. *Prog. Surf. Sci.* **1995**, 49, 331–452.
- (57) Huang, Y. F.; Kooyman, P. J.; Koper, M. T. M. Intermediate Stages of Electrochemical Oxidation of Single-Crystalline Platinum Revealed by in Situ Raman Spectroscopy. *Nat. Commun.* **2016**, *7*, No. 12440.
- (58) Angerstein-Kozlowska, H.; Conway, B. E.; Sharp, W. B. A. The Real Condition of Electrochemically Oxidized Platinum Surfaces Part I\*. Resolution of Component Processes. *J. Electroanal. Chem. Interfacial Electrochem.* **1973**, 43, 9–36.
- (59) Yang, X.; Nash, J.; Oliveira, N.; Yan, Y.; Xu, B. Understanding the PH Dependence of Underpotential Deposited Hydrogen on Platinum. *Angew. Chem., Int. Ed.* **2019**, *58*, 17718–17723.
- (60) Jacobse, L.; Rost, M. J.; Koper, M. T. M. Atomic-Scale Identification of the Electrochemical Roughening of Platinum. *ACS Cent. Sci.* **2019**, *5*, 1920–1928.

- (61) Batista, E. A.; Malpass, G. R. P.; Motheo, A. J.; Iwasita, T. New Insight into the Pathways of Methanol Oxidation. *Electrochem. Commun.* **2003**, *5*, 843–846.
- (62) Bard, A.; Faulkner, L. Electrochemical Methods, 2nd ed.Harris, D.; Swain, E.; Aiello, E., Eds.; John Wiley & Sons, Inc., 2001.
- (63) Merkel, T. C.; Bondar, V. I.; Nagai, K.; Freeman, B. D.; Pinnau, I. Gas Sorption, Diffusion, and Permeation in Poly-(Dimethylsiloxane). *J. Polym. Sci., Part B: Polym. Phys.* **1999**, 38, 415–434.
- (64) Bau, J. A.; Takanabe, K. Ultrathin Microporous SiO2 Membranes Photodeposited on Hydrogen Evolving Catalysts Enabling Overall Water Splitting. ACS Catal. 2017, 7, 7931–7940.
- (65) Yasuda, H.; Stone, W. Permeability of Polymer Membranes to Dissolved Oxygen. J. Polym. Sci., Part A-1: Polym. Chem. 1966, 4, 1314–1316.
- (66) Godet, J.; Pasquarello, A. Proton Diffusion Mechanism in Amorphous SiO2. *Phys. Rev. Lett.* **2006**, 97, No. 155901.
- (67) Kurtz, H. A.; Karna, S. P. Proton Mobility in A-SiO2. *IEEE Trans. Nucl. Sci.* **1999**, 46, 1574–1577.
- (68) Dalstein, L.; Potapova, E.; Tyrode, E. The Elusive Silica/Water Interface: Isolated Silanols under Water as Revealed by Vibrational Sum Frequency Spectroscopy. *Phys. Chem. Chem. Phys.* **2017**, *19*, 10343–10349.
- (69) Lockwood, G. K.; Garofalini, S. H. Bridging Oxygen as a Site for Proton Adsorption on the Vitreous Silica Surface. *J. Chem. Phys.* **2009**, *131*, No. 074703.
- (70) Fogarty, J. C.; Aktulga, H. M.; Grama, A. Y.; van Duin, A. C. T.; Pandit, S. A. A Reactive Molecular Dynamics Simulation of the Silica-Water Interface. *J. Chem. Phys.* **2010**, *132*, No. 174704.
- (71) Tocci, G.; Michaelides, A. Solvent-Induced Proton Hopping at a Water-Oxide Interface. *J. Phys. Chem. Lett.* **2014**, *5*, 474–480.
- (72) Agmon, N. The Grotthuss Mechanism. Chem. Phys. Lett. 1995, 244, 456–462.
- (73) Rimsza, J. M.; Du, J. Nanoporous Silica Gel Structures and Evolution from Reactive Force Field-Based Molecular Dynamics Simulations. *npj Mater. Degrad.* **2018**, *2*, 1–10.
- (74) Cussler, E. L.; Aris, R.; Bhown, A. On the Limits of Facilitated Diffusion. *J. Membr. Sci.* **1989**, *43*, 149–164.
- (75) Harms, C.; Wilhelm, M.; Grathwohl, G. Polysiloxane Based Membranes for High Temperature Polymer Electrolyte Membrane Fuel Cells (HT-PEMFC). ECS Trans. 2009, 1669–1675.
- (76) Robeson, L. M. Correlation of Separation Factor versus Permeability for Polymeric Membranes. *J. Membr. Sci.* **1991**, *62*, 165–185.
- (77) Freeman, B. D. Basis of Permeability/Selectivity Tradeoff Relations in Polymeric Gas Separation Membranes. *Macromolecules* **1999**, 32, 375–380.
- (78) Park, H. B.; Kamcev, J.; Robeson, L. M.; Elimelech, M.; Freeman, B. D. Maximizing the Right Stuff: The Trade-off between Membrane Permeability and Selectivity. *Science* **2017**, *356*, No. eaab0530.
- (79) Henry, J. P.; Chennakesavan, B.; Smith, J. M. Diffusion Rates in Porous Catalysts. *AIChE J.* **1961**, *7*, 10–12.
- (80) Shentu, B.; Nishide, H. Facilitated Oxygen Transport Membranes of Picket-Fence Cobaltporphyrin Complexed with Various Polymer Matrixes. *Ind. Eng. Chem. Res.* **2003**, *42*, 5954–5958.
- (81) Lin, C.; Stedronsky, E. R.; Regen, S. L. PKa-Dependent Facilitated Transport of CO2 across Hyperthin Polyelectrolyte Multilayers. ACS Appl. Mater. Interfaces 2017, 9, 19525–19528.
- (82) McDanel, W. M.; Cowan, M. G.; Chisholm, N. O.; Gin, D. L.; Noble, R. D. Fixed-Site-Carrier Facilitated Transport of Carbon Dioxide through Ionic-Liquid-Based Epoxy-Amine Ion Gel Membranes. J. Membr. Sci. 2015, 492, 303–311.
- (83) Esposito, D. V. Membraneless Electrolyzers for Low-Cost Hydrogen Production in a Renewable Energy Future. *Joule* **2017**, *1*, 651–658.
- (84) Davis, J. T.; Qi, J.; Fan, X.; Bui, J. C.; Esposito, D. V. Floating Membraneless PV-Electrolyzer Based on Buoyancy-Driven Product Separation. *Int. J. Hydrogen Energy* **2018**, *43*, 1224–1238.

- (85) Ooka, H.; Figueiredo, M. C.; Koper, M. T. M. Competition between Hydrogen Evolution and Carbon Dioxide Reduction on Copper Electrodes in Mildly Acidic Media. *Langmuir* **2017**, *33*, 9307–9313.
- (86) Buckley, A. K.; Lee, M.; Cheng, T.; Kazantsev, R. V.; Larson, D. M.; Goddard, W. A.; Toste, F. D.; Toma, F. M. Electrocatalysis at Organic-Metal Interfaces: Identification of Structure-Reactivity Relationships for Co2 Reduction at Modified Cu Surfaces. *J. Am. Chem. Soc.* **2019**, *141*, 7355–7364.